

Synthesis by co-precipitation method, structural and optical properties of ZnO and nickel doped ZnO nanoparticles

P.Geetha Devi¹, A.Sakthi Velu²,

Assistant Professor, Dept of Physics, M.A.M College of Engineering, Siruganur, Tiruchirappalli.

Assistant Professor, PG & Research Department of Physics, Periyar E.V.R. College (Autonomous), Trichy-620023.

Abstract

The structural and optical properties of Ni doped ZnO nanoparticles (NPs) prepared by co-precipitation method have been investigated. The X-ray diffraction pattern confirmed synthesized nanoparticles retained the wurtzite hexagonal structure. From FESEM studies, ZnO and Ni doped ZnO NPs showed Spherical & nanorod mixed phase morphology for undoped and Ni doped ZnO NPs respectively. The amount of dopant (Ni^{2+}) incorporated into ZnO sample was determined by EDAX. The FT-IR spectra confirmed the Zn-O stretching bands at 444 and 451cm^{-1} for ZnO and Ni doped ZnO NPs. Optical absorption measurements show an absorption peak at 376 and 374 nm which was due to excitonic absorption of the pure ZnO and Ni doped ZnO NPs respectively. The photoluminescence measurements revealed that the broad emission was composed of seven different bands due to zinc vacancies, oxygen vacancies and surface defects.

Introduction

Semiconductor nanoparticles (SNP) are gaining much attention due to its peculiar physical and chemical properties which are size and environment (where the particles suspended) tunable [1]. Metal oxide nanoparticles (NPs) are widely used in commercial products such as catalysts, cosmetics, microelectronic devices, semiconductors, sporting goods, and textiles.

Owing to their small size and large specific surface area, NPs exhibit unique physicochemical properties that may differ dramatically from their bulk counterparts. For example, zinc oxide (ZnO) NPs efficiently absorb ultraviolet light and are also highly transparent to visible light, but larger submicrometer and micrometer-sized ZnO particles do not have this combination of properties. Thus, ZnO NPs have been widely used in products where UV protection from a

transparent coating is required, such as in varnishes to protect wood and sunscreens to protect skin.

The synthesis of size and shape-controlled metal oxide nanostructures is very important in controlling their physical and chemical properties for their potential applications. The optical properties of nanocrystalline semiconductors have been studied extensively in recent years. As the size of the material becomes smaller and the band gap becomes larger, this changes the optical and electrical properties of the material, making it suitable for new applications and devices. Among them, the widely accepted method to modify the electrical and optical properties of a semiconductor is the addition of impurity atoms, or doping [2-5]. The antibacterial efficiency of ZnO NPs generally depends on the presence of more ROS, which is mainly attributed to the larger surface area, an increase in oxygen vacancies, the diffusion

ability of the reactant molecules, the release of Zn^{2+} [6] and increase lattice constant 'c' values, due to generation of more hydrogen peroxide (H_2O_2) [7].

In the present investigation, ZnO and Ni doped ZnO NPs are synthesized by co-precipitation method. We have studied the structural and optical properties of the ZnO and Ni doped ZnO NPs.

Experimental and methods

The experimental procedure for the preparation of ZnO and Ni doped ZnO is as follows: 0.1M of Zinc nitrate hexahydrate and 0.8M of NaOH were separately dissolved in each 100 ml of distilled water using two 100 ml beakers. Then, NaOH solution was added drop wise to the Zinc nitrate solution which yielded a white precipitate. The solution with the white precipitate was stirred at room temperature for 6 h. This solution was refluxed for 24 h. Then, a clear solution was obtained, which found to be stable at ambient condition. Thereafter, the solution was washed several times with double distilled water and ethanol. Finally, the precipitate was dried at $120^\circ C$. Thus, ZnO nanopowder was obtained. Similarly, Ni doping on ZnO was done as following 0.003M Nickel nitrate solution was added into 0.097M Zinc nitrate solution. Then 0.8M of NaOH solution was added drop-wise in the above mentioned solutions. The solution with the blue precipitate was stirred at room temperature for 6 h. This solution was refluxed for 24 h. Then, a clear solution was obtained, which found to be stable at ambient condition. Thus, pure ZnO and Ni doped ZnO NPs samples were obtained. These samples were annealed at $700^\circ C$ for 5 h. The annealed samples were used for further analysis. The ZnO and Ni doped ZnO NPs were characterized by X-ray diffractometer (model: X'PERT PRO PANalytical). The diffraction patterns were recorded in the range of 20° - 80° for the ZnO samples where the

monochromatic wavelength of 1.5405 \AA was used. The samples were analyzed by FESEM (model: SUPRA 55) with EDAX (model: ULTRA 55). The FT-IR spectra were recorded in the range of 400 - 4000 cm^{-1} by using Shimadzu IR Affinity-1S spectrometer. The UV-Vis spectra were recorded in the wavelength range 190 - 1110 nm by using Lambda 35 UV-Vis spectrophotometer. The photoluminescence (PL) measurement was

$$\frac{1}{d^2} = \frac{4}{3} \left(\frac{h^2 + hk + k^2}{a^2} \right) + \frac{l^2}{c^2} \quad (1)$$

performed on a (450W high pressure Xenon lamp as the excitation source, Photomultiplier, range 325 - 550 nm record for Horiba Jobin Yvon spectrofluorometer (model: FLUOROMAX-4).

Results and discussion

X-ray diffraction studies

Figure 1(a) shows the XRD patterns of synthesized pure ZnO and Ni doped ZnO NPs. The intense and sharp diffraction peaks suggest that the pure and Ni-doped ZnO NPs are highly crystalline in nature. The standard diffraction peaks show the hexagonal wurtzite structure for the pure ZnO NPs (space group: P63mc). This is also confirmed by the JCPDS data (card no. 36-1451). Interestingly doping of Ni^{2+} shows no additional peaks, which confirms no additional impurity phase formation. A negligible shift is also obtained in the peaks for the ZnO samples doped with Ni^{2+} compared to the pure ZnO sample (see **Fig. 1b**). This shift also corresponds to the strain of the replacement of Zn^{2+} with Ni^{2+} in each compound due to the effect of the ionic radii of the respective metal ions. The lattice constants 'a' and 'c' of wurtzite structure can be calculated by using the relation [8]

With the first order approximation ($n=1$) for the (100) plane the lattice constant

'a' is obtained through the relation $a = \frac{\lambda}{\sqrt{3} \sin \theta}$ and the lattice constant 'c' can be derived for the plane (002) by the relation $c = \frac{\lambda}{\sin \theta}$. The calculated values are 'a' and 'c' for pure ZnO NPs 3.2502 Å and 5.2081 Å respectively. Pure ZnO as compare to the Ni doped ZnO NPs, Ni doped ZnO NPs lattice constant values are increase as shown in the Table 1. The change in the lattice parameter values can be ascribed by the substitution of Ni²⁺ ion in Zn²⁺ sites, which has a higher ionic radius than Zn²⁺ in their tetrahedral coordinates.

The micro-strain analysis is performed for the samples from the X-ray diffraction. The breadth of the Bragg peak is a combination of both instrument and sample-dependent effects. To decouple these contributions, it is necessary to collect a diffraction pattern from the line broadening of a standard material such as silicon to determine the instrumental broadening. The instrument-corrected broadening β_{hkl} [9] can be represented by:

$$\beta_{hkl} = [\beta_{hkl}^2 \text{ measured} - \beta_{hkl}^2 \text{ instrumental}]^{1/2} \quad (2)$$

The particle grain size of pure ZnO NPs is determined by the X-ray line broadening method using the Scherrer's equation,

$$D = \frac{k\lambda}{\beta_D \cos \theta} \quad (3)$$

where D-is the size in nanometers, λ is the wavelength of the radiation (1.5406Å for CuK α), k is a constant (0.94), β_D -is the peak width at half-maximum intensity and θ is the peak position.

The average crystallite size of pure ZnO NPs is found to be 35 nm. The average crystallite size (**Table 1**) decreases in the Ni²⁺ doped ZnO NPs. The reduction in the particle size is mainly due to the distortion in the host ZnO lattice by the foreign impurities *i.e.*, Ni²⁺,

which decrease the nucleation and subsequent growth rate of the ZnO NPs.

The strain-induced broadening β_ϵ is given by the Wilson formula $\beta_\epsilon = 4\epsilon \tan \theta$, where ϵ is the root mean square value of the micro-strain. Assuming that the particles size and strain contributing to the line broadening and independent of each other and both have a Cauchy like profile, the observed line width is simply the sum of these two, *i.e.*, $\beta_{hkl} = (k\lambda / D \cos \theta) + 4\epsilon \tan \theta$, which becomes as

$$\beta_{hkl} \cos \theta = \left(\frac{k\lambda}{D} \right) + 4\epsilon \sin \theta \quad (4)$$

When plotting the Williamson-Hall equation between $\beta \cos \theta$ Vs. $4\sin \theta$, the slope of the line is the strain ϵ . **Figures 1c** show the plots of Williamson-Hall equation for pure ZnO and Ni doped ZnO NPs samples. The calculated strain values are given in **Table 1**. As compared to the pure ZnO NPs, the strain increases in the Ni²⁺ -doped ZnO NPs These effects change the size and shape of the particles.

Field Emission Scanning Electron Microscopic analyses

The FESEM images of the pure ZnO and Co-doped ZnO NPs are shown in **Fig. 2(a-b)**. From the images, we can see that the pure ZnO and Ni doped nanoparticles are found to be spherical and rod like mixed phase formed. The width of the nanorod sizes is found to be 79 nm and 74 nm for pure ZnO and Ni doped ZnO NPs, respectively. The nanorod width decreased of the Ni doped ZnO NPs are found to be reduced as compared to that of pure ZnO NPs. This reduction in width size is due to the distortion in the host material incorporated with Ni²⁺ metal ion in ZnO NPs surface area. Hence the sizes of ZnO NPs are reduced by Ni doping.

Energy Dispersive Analysis X-ray (EDAX) Studies

The chemical composition of the synthesis nanoparticles were analyzed by energy dispersive X-ray spectroscopy (EDX). From the EDX spectra of the undoped and Ni doped ZnO NPs are shown in Fig. 3(a-b). In the doped samples, the concentrations of Ni are found to be 3.90% respectively. In the pure ZnO Samples, the chemical compositions of Zn and O are found to be 56.42% and 43.58% respectively. In case of Ni doped ZnO NPs, as compared to pure ZnO NPs oxygen atomic percentage increase and decrease the Zinc atomic percentage. Whereas 49.75% and 46.35% are Ni doped ZnO NPs respectively. While this change due to the effect of Ni²⁺ ions in the Zn-O lattice.

FT-IR spectroscopic studies

The FT-IR spectra of the prepared ZnO and Ni doped ZnO NPs are shown in Fig. 4. The broad absorption bands at 3429 and 3436 cm⁻¹ are observed at hydroxyl groups of absorbed water molecules or Zn-OH for undoped and Ni doped ZnO NPs respectively. The peaks at 2923 cm⁻¹ are due to asymmetric C-H bonds [5]. At 2910 cm⁻¹, the sharp intensity of the asymmetric stretching mode of the CH₂ groups in PEG can also be observed for pure ZnO NPs. The sharp absorption band were observed around 1547 and 1540 cm⁻¹ for pure ZnO and Ni doped ZnO NPs respectively, which shows the presence of asymmetric stretching mode vibration of C=O bands [10]. The symmetric C=O bands are observed at 1432 and 1439 cm⁻¹ for the pure ZnO and Ni doped ZnO samples respectively. The C-H

Photoluminescence study

In general, the photoluminescence spectra observed in ultraviolet (UV) and visible emission in ZnO NPs samples. The UV emission is due to near band-edge emission and the visible emission is due to different intrinsic defects such as oxygen vacancies (V_o), Zinc Vacancies (V_{zn}), Oxygen interstitials (O_i), Zinc interstitials (Zn_i) and oxygen antisties (O_{zn}) [15].

out-of plane bending bands are observed 883 and 891 cm⁻¹ for undoped and doped ZnO samples. The Zn-O stretching bands appear at 444 and 451 cm⁻¹ for the respective ZnO NPs.

UV-Visible spectroscopic studies

The UV-Vis absorption spectra, peaks are found at 376 and 374 nm for pure ZnO and Ni doped ZnO NPs respectively. The position of the absorption spectra is observed to shift toward the lower wavelength side for Ni doped ZnO NPs. This indicates that the band gap of ZnO material increases with the doping of Ni²⁺ ions. The increase in the band gap or blue shift can be explained on the basis of the Burstein-Moss effect [11]. While the Fermi level shifts close to the low energy transitions are blocked and the value of the band gap increase [12].

The optical band gap is determined by Tauc model [13]. $\alpha h\nu = A(h\nu - E_g)^n$ Where E_g is the optical band-gap. A is a constant and the exponent n depends on the transition. The value of (n = 1/2, 3/2, 2, or 3) depends on the nature of the electronic transition (1/2 for allowed direct transition, 2 for allowed indirect transition, 3/2 and 3 for forbidden direct and forbidden indirect transitions, respectively). Relation between $(\alpha h\nu)^2$ and photon energy (hν) is plotted and shown in Fig. 5. The band gaps of 3.3 eV and 3.315 eV are obtained for pure ZnO and Ni-doped ZnO NPs respectively. The pure ZnO NPs as compared to Ni doped ZnO NPs, band gap slightly increase the Ni doped ZnO NPs. This is also in good agreement to the quantum confinement effect of the nanoparticles [14].

The photoluminescence spectra of the synthesized pure ZnO and Ni doped ZnO NPs samples recorded at the excitation wavelength of 350nm are shown in Fig. 6(a-b)). The PL emission is observed for all of the samples, from the very short wavelength of 325 nm to the longer wavelength of 550 nm. A good fit with seven peaks using Gaussian function is obtained for all of the PL spectra of the samples, labeled as K1, K2, K3, K4, K5, K6 and K7 (see **Fig. 6a-b**) The solid lines represent the linear combination of the ten Gaussian peaks. K1 has the shortest wavelength and K7 has the longest wavelength.

In the present case, the near band emissions (K1, K2 and K3) are located in the UV region (349 nm, 364 nm & 397 nm) for the pure ZnO NPs. This UV peak corresponds to the radiative recombination of the free exciton-exciton collision process in the ZnO NPs. The violet emission K4 at 423 nm is ascribed to an electron transition from a shallow donor level of natural Zn_i to the top level of the valence band [16].

The K5 and K6 peaks are the origin of the blue emission centered at 443 nm and 458 nm are attributed to singly ionized Zn vacancies [17]. There is blue-green emission bands K7 at 484 nm due to a surface defects in the ZnO NPs corresponding to the transition between oxygen vacancy and oxygen interstitial defect.

The values of emission bands K1, K2, K3, K4, K5, K6 and K7 (Fig. 6b) of the Ni-doped ZnO NPs are given in Table 2. From the Ni doped ZnO NPs, the blue band (K6) and blue-green band (K7) emissions as compare to the pure ZnO NPs, Ni doped ZnO NPs emission were increases due to the distortion in the host ZnO lattice by the Ni ion impurities. These changes in the emissions confirm the substitution of the Ni²⁺ into the ZnO lattice.

Sample	Lattice Parameter values (Å)		Average Crystallite size D (nm)	Micro-strain ε
	a	c		
ZnO	3.2502	5.2081	35	0.00252
ZnO:Ni	3.2503	5.2088	32	0.00658

Table 1 The sizes of pure ZnO and Ni-doped ZnO Ps

Fitting	ZnO (nm)	ZnO:Ni (nm)
K1	349	349
K2	364	364
K3	397	396
K4	423	423
K5	443	443
K6	458	460
K7	484	491

Table 2 Comparison of the PL emission values of the pure ZnO and Ni-doped ZnO NPs

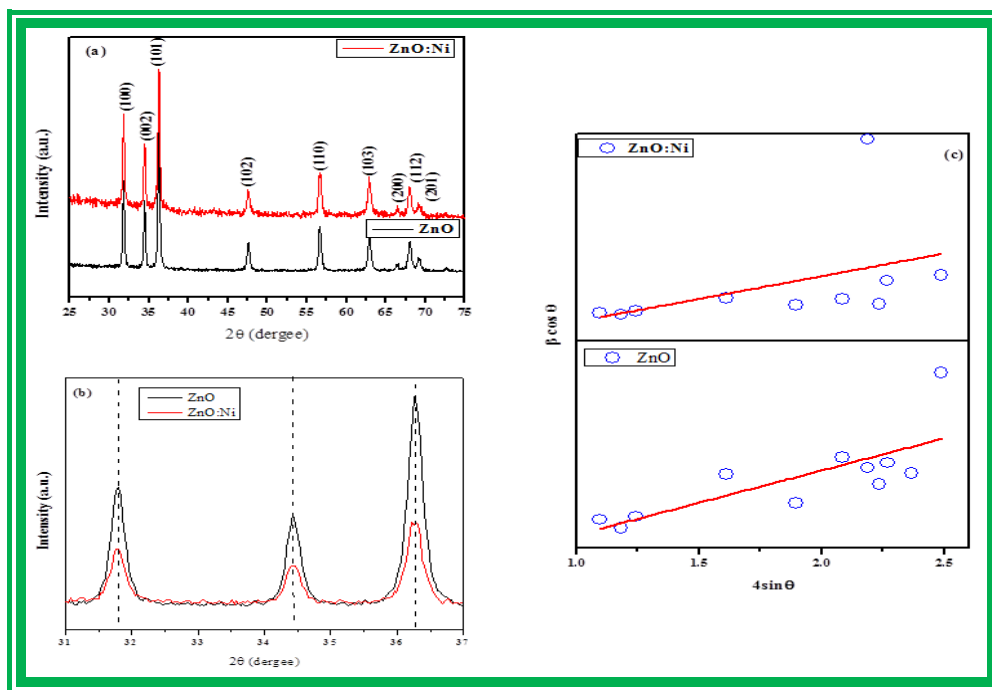


Figure 2.2 X-ray powder diffraction patterns of (a) pure ZnO and Ni doped ZnO NPs (b) Doping-induced peak shift for pure ZnO and Ni-doped ZnO NPs and (c) Williamson-Hall plots of pure ZnO and Ni doped ZnO NPs.

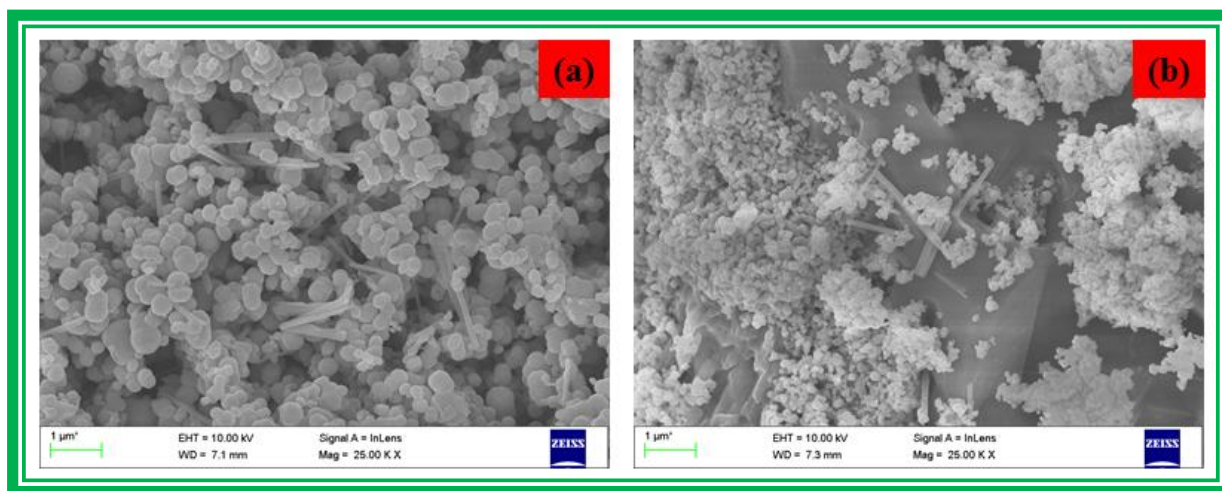


Figure 2 FESEM image of (a) pure ZnO, and (b) Ni doped ZnO NPs.

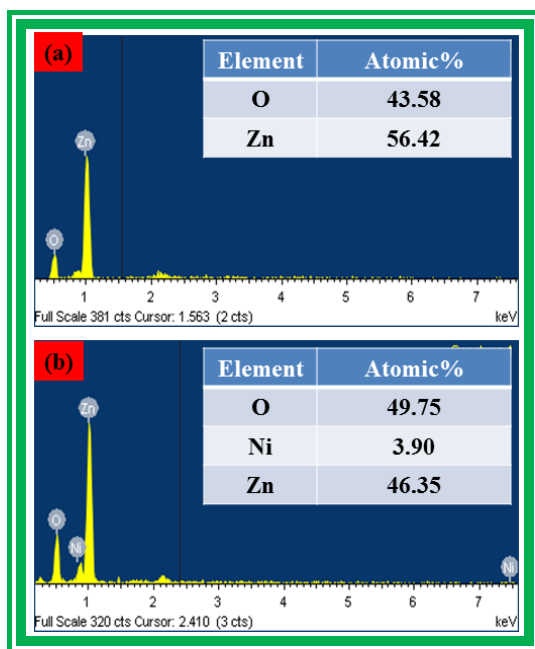


Figure 3 EDAX spectra of (a) pure ZnO, and (b) Ni doped ZnO NPs.

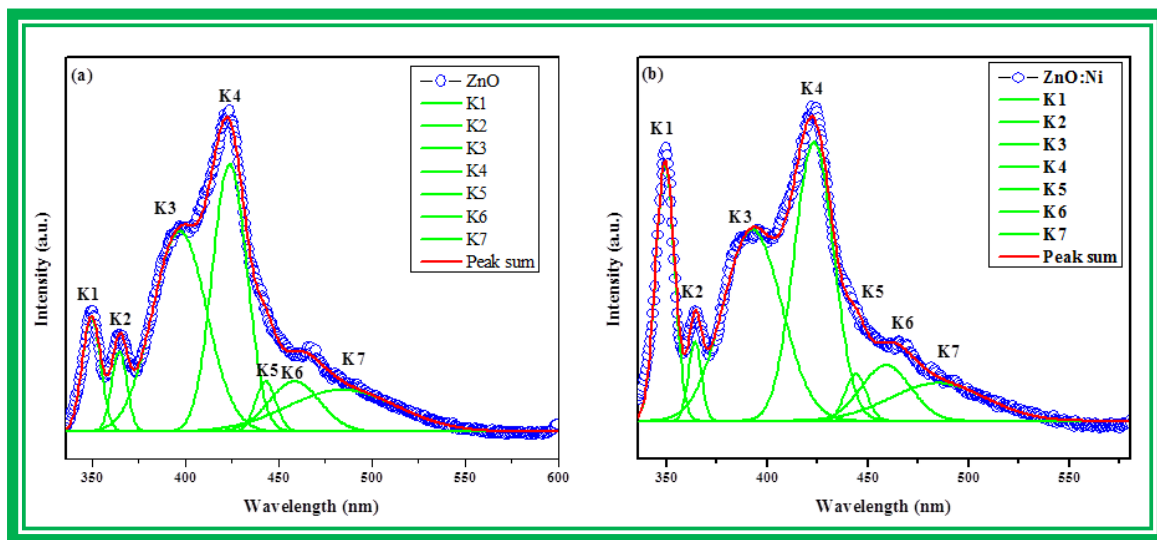


Figure 6 Gaussian de-composed photoluminescence emission spectra of
 (a) Pure ZnO NPs and (b) Ni doped ZnO NPs.

Conclusion

In conclusion, pure ZnO and Ni doped ZnO NPs samples were synthesized by co-precipitation method. The X-ray diffraction study confirmed that the prepared particles

were of the hexagonal wurtzite structure. The average crystallite size of pure ZnO and Ni doped ZnO NPs were found to be 35 and 32 nm. The average crystallite size decreases in the Ni²⁺ doped ZnO NPs. The reduction in the particle size was mainly due to the distortion

in the host ZnO lattice by the foreign impurities *i.e.*, Ni²⁺, which decrease the nucleation and subsequent growth rate of the ZnO NPs. Pure ZnO NPs as compare to the Ni doped ZnO NPs, Ni doped ZnO NPs lattice constant values were increased. From the images, we can see that the pure ZnO and Ni doped NPs were found to be spherical and rod like mixed phase formed. From the EDAX analysis, the chemical compositions were estimated for the prepared samples. The UV-Vis spectra, the optical band gaps were found to be 3.3 eV and 3.315 eV for pure ZnO and Ni-doped ZnO NPs respectively. From the Ni

doped ZnO NPs, the blue emission and blue-green emissions as compared to the pure ZnO NPs, Ni doped ZnO NPs emissions were increased due to the distortion in the host ZnO lattice by the Ni ion impurities. These changes in the emissions confirm the substitution of the Ni²⁺ into the ZnO lattice. In antimicrobial application, increasing lattice constant, decrease particles size, increasing oxygen vacancies, due to more production of reactive oxygen species (ROS). The more ROS production means, increasing antimicrobial efficiency. So that reason Ni doped ZnO NPs were used in the microbial applications.

References

- [1] A. B. Djurii, Y. H. Leung, *Small*, 2 (2006) 944-961.
- [2] L. S. Hsu, C. S. Yeh, C. C. Kuo, B. R. Huang, S. Dhar, *J. Optoelectron. Adv. Mater.*, 7 (2005) 3039-3046.
- [3] R. N. Bhargava, D. Haranath, A. Metha, *J. Korean Phys. Soc.*, 53 (2008) 2847-2851.
- [4] S. Y. Bae, C. W. Na, J. H. Kang, J. Park, *J. Phys. Chem. B*, 109 (2005) 2526-2531.
- [5] A. S. Haja Hameed, C. Karthikeyan, S. Sasikumar, V. Senthil Kumar, S. Kumaresan, G. Ravi, *J. Mater. Chem. B*, 1 (2013) 5950-5962.
- [6] J. Becker, K. R. Raghupathi, J. S. Pierre, D. Zhao R. T. Koodali, *J. Phys. Chem. C*, 115 (2011) 13844-13850.
- [7] O. Yamamoto, M. Komatsu, J. Sawai, E. Z. Nakagawa, *J. Mater. Sci. Mater. Med.*, 15 (2004) 847-851.
- [8] C. Suryanarayana, M. Grant Norton, *X-ray Diffraction: A Practical Approach*, Plenum Press, New York, 1998.
- [9] Ramakanth, K., *Basics of diffraction and its application*, I. K. International Publishing house PVT. LTD. New Dehli, 2007.
- [10] S. S. Alias, A. B. Ismail, A. A. Mohamad, *J. Alloys. Comp.*, 499 (2010) 231.
- [11] S. Suwaboon, T. Ratana, W. T. Ratana, *J. Sci. Technol.*, 4 (2007) 111-121.
- [12] M. Arshad, A. Azam, A. S. Ahmed, S. Mollah, A. H. Naqvi, *J. Alloys comp.*, 509 (2011) 8378-8381.
- [13] S. T. Tan, B. J. Chen, X. W. Sun, W. J. Fan, H. S. Kwok, X. H. Zhang, S. J. Chua, *J. Appl. Phys.* 98 (2005) 013505-5
- [14] T. Takagahara, K. Takeda, Theory of the quantum confinement effect on excitons in quantum dots of indirect-gap materials, *Phys. Rev. B*, 46 (1992) 15578-15581.
- [15] P. Mishra, R. S. Yadav, A. C. Pandey, *Struct. Chem.*, 22 (2011) 1281-1286.
- [16] X. M. Fan, J. S. Lian, L. Zhao, Y. Liu. *Appl. Surf. Sci.*, 252 (2005) 420.
- [17] S. K. Mishra, R. K. Srivastava, S. G. Prakash, R. S. Yadav, A. C. Panday, *Opto-Electron. Rev.*, 18 (2010) 467-473.